ICAS 2021 SHANG HAI
32nd Congress of the International Council of the Aeronautical Sciences
September 6-10, 2021 Pudong Shangri-La, Shanghai, China

ENERGY HARVESTING FROM PIEZOELECTRIC FRINGES AT THE TRAILING-EDGE OF A FINITE WING WITH LEADING-EDGE TUBERCLES

E.P. Pereira[1], A. Esmaeili[2] & J.M.M. Sousa[1]

[1]IDMEC, Instituto Superior Técnico, Universidade Técnica de Lisboa, Av. Rovisco Pais, 1049-001 Lisboa, Portugal
[2]Mechanical Engineering Department, Faculty of Engineering, Ferdowsi University of Mashhad, Iran

Abstract

At present time, the use of fixed-wing Micro Aerial Vehicles (MAV) is challenged by limited operation windows due to weight restrictions on the batteries and the decreased performance due to early onset of stall at high angles of attack. Aiming to overcome this problem, a hybrid active-passive stall control system was previously proposed for a wing with leading-edge tubercles. However, the active control system requires additional power, which is problematic with current batteries due to their excessive weight. Hence, this work focused on the feasibility of mounting a fringe-type piezoelectric device at the trailing-edge of the wing for energy harvesting. The device oscillates with the shedding of the vortices from the tubercled wing to power the active stall control system. A physical model was explored to find the device whose resonant frequency matched best the vortex shedding frequency of the wing. Another model was used to predict the voltage output of the device operating at this frequency. Based on the results of the former, selected devices were put to the test in a wind tunnel. The power density ratio harvested by the most promising device ranged 10^{-5} W/kg for a light weight of about 50 mg. The voltages in closed-circuit were observed to be in the order of 60 mV, with the open-circuit voltages reaching 300 mV. Additionally, the wing with the piezoelectric fringe has shown to be able of producing a slightly higher lift-to-drag ratio than the clean wing at high incidence.

Keywords: energy harvesting; piezoelectric fringes; tubercled wing; stall control; wake sensing.

1. General Introduction

Being wary about the effects of fossil fuels on the climate and human health, finding alternative ways to re-use ambient energy is vital to power aircraft in the future. Internal combustion engines powered by fossil fuels are steadily becoming obsolete in most of the transport sector, with aviation being the one sector lagging behind. This change is nevertheless already hitting the aviation industry, with new all-electric light aircraft being launched in the upcoming years. However, the utilization of electric propulsion appears to be only feasible on its own for relatively low-autonomy missions, due to weight restrictions by the battery packs. Hence, harvesting ambient energy such as solar, thermal, wind, acoustic waves, or mechanical vibrations is crucial to enhancing the range of aircraft, with each one of these choices carrying on pros and cons in different mission types. For example, energy might be harvested from the structural vibrations or from vortices in the flow around a wing to power certain on-board systems. After optimization, such concept could eventually be used to power the propulsion system of small flying vehicles.

1.1 State-of-the-Art

Flow energy harvesters have been thoroughly studied in recent years. The most usual investigations involve the configuration of a flapping beam subjected to axial flow, fixed at the leading-edge and free to flap at its trailing-edge. These harvesters oscillate due to the de-stabilizing fluid forces being attenuated by the stabilizing elastic force of the beam (structural stiffness). The oscillations can then be self-sustained if a critical velocity value is reached. Several analyzes [1-3] proposed numerical models to predict the behavior of the beam in flutter boundary and post-critical conditions. However, not much is found in the literature about energy harvesting in the wake of fixed-wings or airfoils, and most of those are numerical studies [4], or morphing-wing studies [5-6].

Energy harvesting from mechanical vibrations using a piezoelectric beam mounted inside a MAV wing prototype was investigated earlier [7], as illustrated in Figure 1. The goal was to harness enough energy to power an active stall control system, adding to a passive control technique based on a leading-edge modification of a NASA LS(1)-0417 wing, which in turn was inspired by the tubercles found in humpback whale's flippers. In this investigation, peak power values ranging 20 to 30 μW for a device weighing approximately 10 g were obtained. Another related study [8] was able to achieve 15 mW/cm^3 with a tuned device, albeit without considering the weight of the device on the power output. A similar work [9] in which the dielectric properties of a Polyvinylidene Fluoride (PVDF) were tuned with nanocomposites to optimize energy harvesting was also reported in the literature. In the latter case, the maximum power harvested was 36 nW.

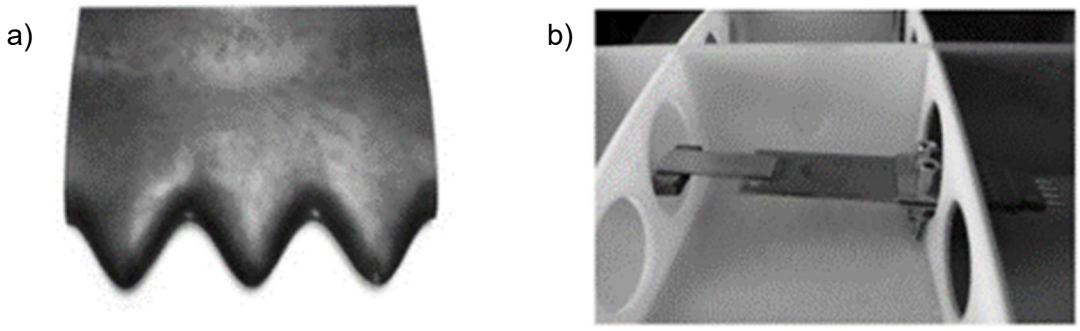

Figure 1 – Modified NASA LS(1)-0417 wing (aspect ratio 1.5) for vibration energy harvesting [7]: a) leading-edge modification (tubercles); b) piezoelectric beam device mounted inside the wing.

More recently, a study on energy harvesting from vortex-induced vibrations using a piezoelectric flag in an inverted configuration, placed in the wake of a NACA0012 airfoil and a SD7003 airfoil, was also conducted [10]. These authors have concluded that, for the Reynolds numbers tested, the voltage was highest at a certain position in the wake of the airfoils, above and downstream of the trailing-edge. They also concluded that using such a device for wake sensing is viable, while not disturbing the wing itself.

2. Piezoelectric Energy Harvesting

Structural vibrations are present everywhere, with the structures themselves being built in a way that prevents those vibrations from destroying the structure. The concept of vibrational energy harvesting consists in converting these vibrations into electrical energy. With the rise of micro-electro-mechanical system devices, the interest in this type of energy harvesting has grown exponentially due to the amounts of energy that may be harvested versus the cost and weight of such devices [8]. This process is done in two steps, as follows: first, a mechanical-to-mechanical conversion is carried out, usually through a mass-spring system, which is followed by a conversion to electricity by a mechanical-to-electrical converter. The need of a mass-spring system is primarily a consequence of the small amplitude exhibited by ambient vibrations. Nevertheless, these can be boosted by the mass-spring system inducing resonance in the mass, thus allowing to maximize the harvested power. Such resonance phenomenon amplifies the amplitude of the mobile mass relative to amplitude of the ambient vibrations [11].

Piezoelectric devices can operate in two ways: mechanical stresses generate an electrical voltage, or an electrical voltage generates mechanical stresses. Thus, these may be used as energy harvesters or as actuators instead. On the other hand, the harvested power of piezoelectric devices is typically sufficient to power most micro-scale electronics [7].

2.1 Piezoelectric Modes

There are two modes in which the electrodes of a piezoelectric device can be configured in: mode [3-1] and mode [3-3]. The configuration is dependent on the direction of the applied strain and the direction of the electric field. These modes have some fundamental differences, which will be briefly presented and explained next.

- Mode [3-1]: This mode is defined by the strain vector being perpendicular to the electric field vector, meaning that the applied force and poling have the same direction.

- Mode [3-3]: This mode is characterized by an applied force being perpendicular to the poling direction, which leads to the electric field and strain vectors being parallel.

2.2 Piezoelectric Constitutive Equations

Piezoelectric materials are dielectric materials. For example, this makes the poled piezoceramics transversely isotropic materials. According to the IEEE Standard on Piezoelectricity [12], constitutive equations [13] can be cast as follows:

$$\begin{aligned} S &= [s^E]T + [d^t]E \\ D &= [d]T + [\epsilon^T]E \end{aligned}, \tag{1}$$

with S and T denoting the strain and stress components, respectively, and E and D standing for to the electric field and the electric displacement components, respectively. The piezoelectric constant is represented by d, while s is the elastic compliance and ϵ is the permittivity constant. Furthermore, superscript E implies strain applied at zero or constant electric field, and superscript T indicates that a parameter is calculated at constant electric displacement. As usual, t stands for the transpose.

3. Modeling and Design

Whereas previous work focused on scavenging energy from mechanical vibrations by placing the piezoelectric harvester inside the wing with leading-edge tubercles [7], the nature of the problem changed when aiming to harvest energy directly from the flow instead, thus involving the installation a piezoelectric device outside the wing. In the former, the frequency at which the device operates is largely independent of the wing incidence at a certain Reynolds number, kept at 140,000 in the mentioned study. As such, the harvester was tuned to match the fundamental frequencies produced by mechanical vibrations in the wing structure. This involved changing the device itself, attaching a steel tip plate and a tip mass to reduce the natural frequency of the commercial device from 110 Hz down to a fundamental frequency of 17.6 Hz quantified via modal analysis of the wing [7].

For the underlying problem, predicting how the harvester will vibrate with the oncoming flow is key to the selection of a device with a design that matches the vortex shedding frequency (vortices are constantly being shed from the leading-edge of the wing due to the tubercles [14]). Fine-tuning a device to match this frequency as it was done before is not efficient, since the added mass involved in this process does not bring any benefits for the whole system. Hence, a numerical model to predict the frequencies involved was formulated.

Prior to the modeling efforts, two configuration options have been considered for the installation of the piezoelectric harvester, taking into account requirements imposed by a practical application. The first option is a piezoelectric fringe mounted at the trailing-edge of an airfoil, as illustrated in Figure 2a; in the second option, the piezoelectric fringe operates as an inverted flag placed above the upper surface of the airfoil (near the trailing-edge), as shown in Figure 2b.

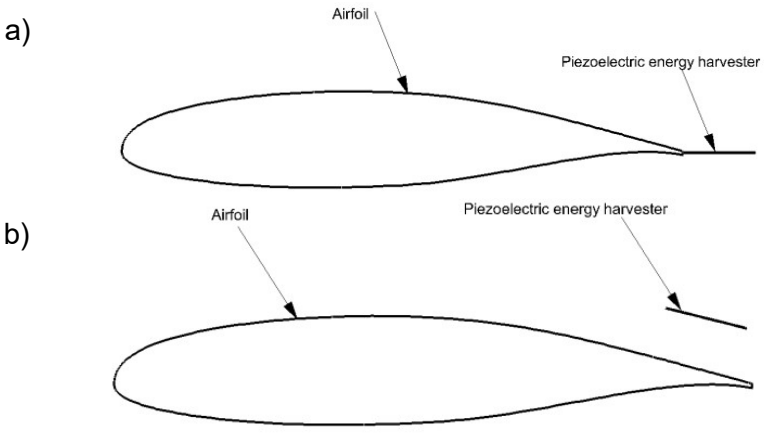

Figure 2 – Configuration options for the installation of the piezoelectric harvester: a) fixed at trailing-edge; b) inverted-flag above the upper surface.

A recent computational fluid dynamics study [15] demonstrated that these two configurations are associated with distinct fundamental frequencies, as portrayed in Figure 3. Hence, the characteristics of the piezoelectric harvester depend on the selected configuration, in order to match the desired frequency. The inverted flag option shows more promise in terms of harvesting the energy from the vortices shed from the leading-edge of the tubercled wing, while also slightly increasing pre-stall and post-stall lift-to-drag ratios. In [15] it was concluded that there was a decrease in lift accompanied by a larger decrease in drag, which resulted in an overall increase of the lift-to-drag ratio. The decrease in drag was related to the resizing of the shed vortices by the piezoelectric fringe, via braking large vortices into smaller ones and thus reducing the overall drag.

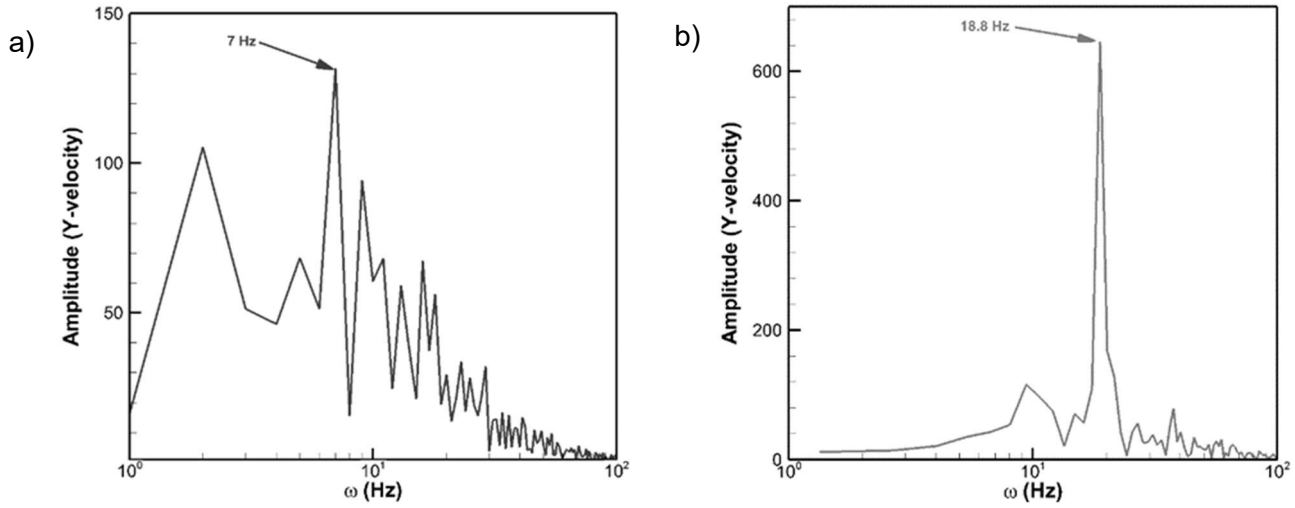

Figure 3 – Frequency analysis [15] of the configuration options: a) fixed at trailing-edge; b) inverted-flag above the upper surface.

3.1 Frequency Model

Apparently emerging as a better option, initial focus was placed on the inverted flag configuration while elaborating the frequency model. In Figure 3b, it can be observed that the vortex shedding frequency lies at 18.8 Hz for this configuration. One must emphasize that the process of harvesting energy from the vortices is not linear, with the highest amount of energy being harvested at the natural frequency ω_n of the device. However, our aim is not to find the device which can harvest the most energy at natural frequencies because the MAV will not be operated at these conditions solely. There is a whole spectrum of flight conditions that need to be considered. By choosing a harvester characterized by a slightly lower natural frequency, energy can be harvested more efficiently at lower air speeds.

Accordingly, the objective of the modeling was set to obtain the material characteristics of the fringe that would vibrate at frequencies in the range of 10 to 15 Hz. The piezoceramic harvester used in [7] to scavenge energy from mechanical vibrations in the wing structure exhibited a natural frequency of 110 Hz, and therefore had to be fine-tuned in order to match the fundamental frequencies of those vibrations. Hence, a device with similar characteristics would not be a viable choice for the current experiments. Adding tuning masses to the MAV is not optimal since the performance gain in energy harvesting is offset by weight penalties incurred with a heavier vehicle. An extensive search for other commercial piezoceramic devices did not yield any results for a natural frequency below 49 Hz. Thus, a different option had to be considered, namely using a PVDF sheet configured in mode [3-1], and eventually glued to a substrate layer if required.

Aiming to predict the vibration frequencies of the piezoelectric fringe, one must analyze the effects controlling this mechanism. As mentioned earlier, the plate is subjected to a de-stabilizing motion by the flow vortices and a stabilizing motion imposed by the plate's structure [10]. The non-dimensional bending stiffness β represents the magnitude of the bending force relative to the fluid inertial force [10,16], and is given by:

$$\beta = \frac{B}{\rho_f U_\infty^2 L^3} \ , \tag{2}$$

where ρ_f is the density of the fluid, and U_∞ denotes de free-stream velocity. In addition, in Eq. (2), L and B stand for the length and the dimensional flexural rigidity of the fringe, respectively. Taking a (single-layer) uniform sheet, the latter parameter which is given by:

$$B = \frac{Et^3}{12(1-\nu^2)} \ , \tag{3}$$

where E is Young's modulus, t denotes the thickness of the fringe and ν stands for the Poisson ratio of the material. On the other hand, for a multi-layer fringe:

$$B = \frac{E_s h_s^3 H}{12(1-\nu_s^2)} + \frac{2E_p h_p H}{1-\nu_p^2}\left(\frac{h_s^2}{4} + \frac{h_s h_p}{2} + \frac{h_p^3}{3}\right) \ , \tag{4}$$

where the subscripts s and p refer to the substrate and the piezoelectric layers, respectively, H is the total width of the fringe, and h denotes the thickness of a layer. While a bimorph harvester is a design to be considered, a unimorph piezoelectric fringe would constitute a simpler option. Following the calculation of B, the fundamental frequency may be estimated [17] from this relation:

$$f = \frac{\omega_n}{2\pi} \approx \frac{3.515}{2\pi L^2}\sqrt{\frac{B}{\mu}} \ , \tag{5}$$

where μ is the mass per unit length of the fringe.

Based on the equations above, a sensitivity study was initially performed, aiming to evaluate how the fundamental frequency changed with respect to the use of different substrate materials, as well as different sizes of fringe length, PVDF thickness, and substrate thickness. An example of the full set of results obtained for various metals (namely Brass, Steel, Aluminium) as substrate material, as well as for the epoxy laminate FR4 and Polyester, is shown in Figure 4 for a bimorph PVDF fringe.

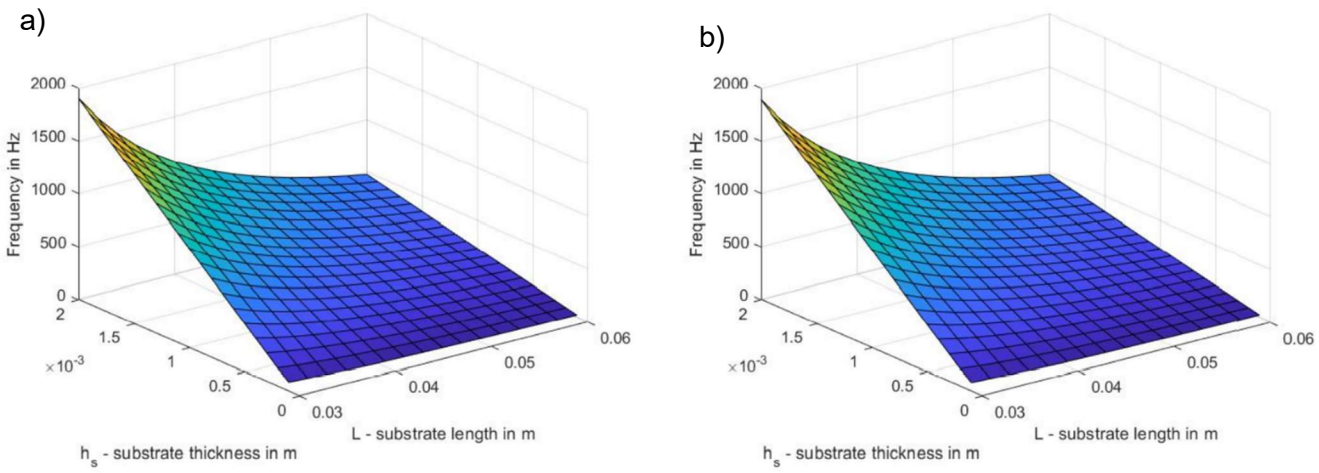

Figure 4 – Sensitivity study of a bimorph fringe with an Aluminium substrate: a) PVDF layer with $h_p = 28$ μm; b) PVDF layer with $h_p = 52$ μm.

The present study showed that, independently of the substrate material, the fundamental frequency is largely impacted by the substrate thickness. Finding commercial solutions of substrate materials with a thickness lower than 0.1 mm is difficult and expensive, so this was the minimum thickness considered in the sensitivity study. This value has proven to be ideal in the scope of the present investigation, since model estimates approximated the frequency range targeted in the beginning of this work. The length of the fringe has some importance, with the difference in fundamental frequency between a short and a long sheet being more accentuated for thicker substrates, but not insignificant for the minimum substrate thickness. However, the thickness of the PVDF has not shown to be of great importance, with similar predicted data (16-23 Hz) except for the use of Polyester as substrate (9 Hz).

Concerning the alternative installation configuration considered in Figures 2a and 3a, the expected natural frequency is even lower than that obtained in the sensitivity study for Polyester, i.e., about 7 Hz. (Cf. Figure 3a). This study did not present any substrates able to achieve such small frequency with the PVDF, thus the option of performing the experiments using a piezoelectric harvester without the use of a substrate was also considered. The frequency model demonstrated that this would be a viable solution for the latter configuration, with an estimate [15] for the fundamental frequency of 7.4 Hz. In fact, from the practical point of view, this configuration presents an easier assembly since an additional support for the fringe is not required, as opposed to the inverted flag configuration, which would bring additional weight and drag penalties into the design.

3.2 Aero-Electro-Mechanical Model

The frequency analysis carried out earlier was critical for the design of the piezoelectric fringes, so that the devices may be expected to operate near optimal conditions. However, predicting the energy harvesting capabilities of such devices is of paramount importance, though it requires a much larger modeling complexity to account for the three physical domains involved (Aerodynamical, Mechanical and Electrical).

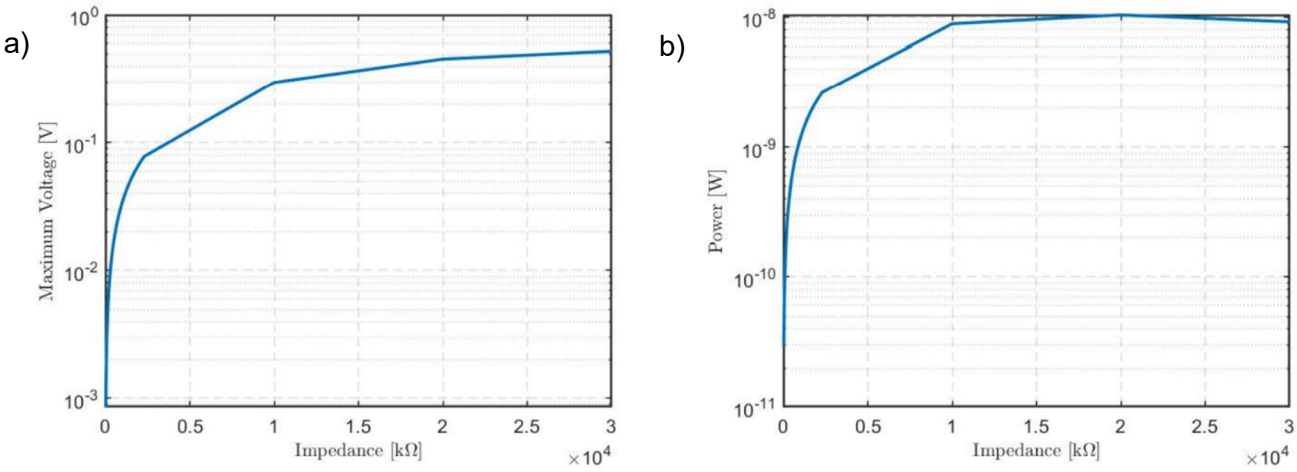

Figure 5 – Results of the aero-electro-mechanical model as a function of circuit impedance for device A (Cf. next chapter): a) voltage output; b) power output.

This model is based on Eq. (1), but several assumptions were made to simplify the problem: a) the harvester is considered to be an uniform Euler-Bernoulli beam of a PVDF sheet (for the inverted flag configuration a composite structure of substrate plus PVDF sheet would be considered); b) the electrical circuit has a resistive load only with the harvester connected to it through the electrodes; c) the electrodes are perfectly conductive and cover the entire bottom and top surfaces of the PVDF sheet so that the electric field may be assumed uniform across the entire beam; d) the beam is continuously oscillated by the fluid flow, hence enabling continuous harvesting of the electrical current; e) the leakage resistance of the PVDF is considered to be negligible, as the PVDF is connected in parallel to the resistive load; f) the piezoelectric constitutive equations generate an electrical capacitance term and will be accounted for in the model equations, albeit not being shown in the circuit as parallel to the resistive load - it is considered as an internal parameter. Additional details about the aero-electro-mechanical model have been given elsewhere [15], and these will be therefore omitted here for the sake of brevity.

The results of the aero-electro-mechanical model for commercial device A, to be presented in the next chapter, are shown in Figures 5 and 6. The first set of data shows the voltage and power outputs of the model as a function of the impedance of the electric circuit. As might be anticipated, the voltage rises quickly at low resistance, reaching a quasi-asymptotic state at high impedances. The harvested power follows a similar trend up until 20 MΩ, where a small increase in voltage output is counteracted by the high impedance. On the other hand, the second set of data, displaying the evolution of both voltage and power as a function of the flow Reynolds number, shows a continuous increase of the harvester outputs with increasing speed (within the investigated range of Reynolds number).

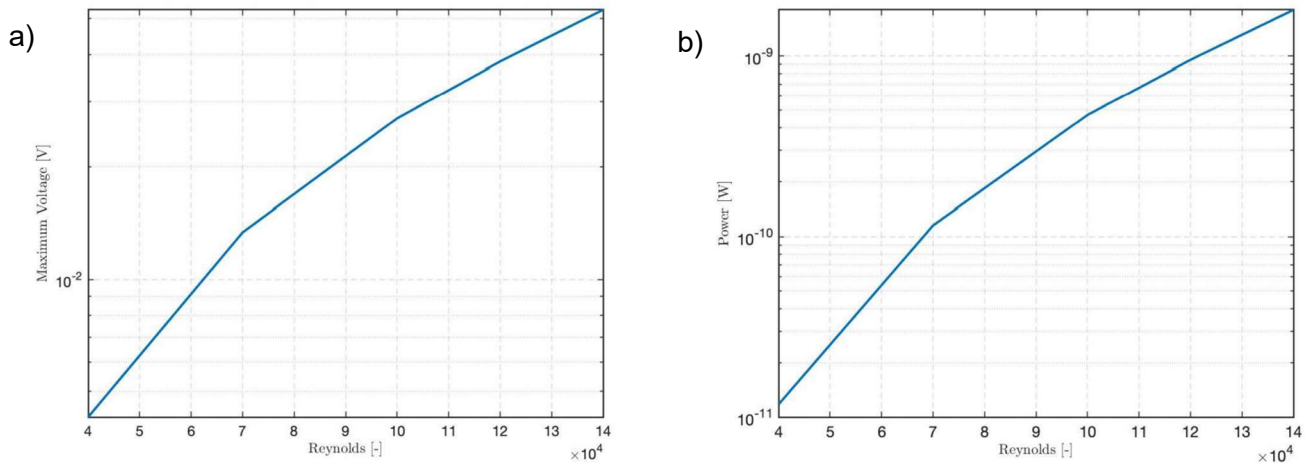

Figure 6 – Results of the aero-electro-mechanical model as a function of Reynolds number for device A (Cf. next chapter): a) voltage output; b) power output.

4. Wind Tunnel Results and Discussion

In this work, three types of commercial piezoelectric devices (Mouser Electronics) were tested. All these correspond to single-layer PVDF devices, without substrate (but including protective coating), differing only in the thickness of the piezoelectric layer and its length. Device A has a piezo-electric layer thickness of 52 μm and a length of 30 mm; device B has the same thickness, doubling in length; device C is 28 μm thick and again 30 mm long (as device A). These can be viewed in Figure 7.

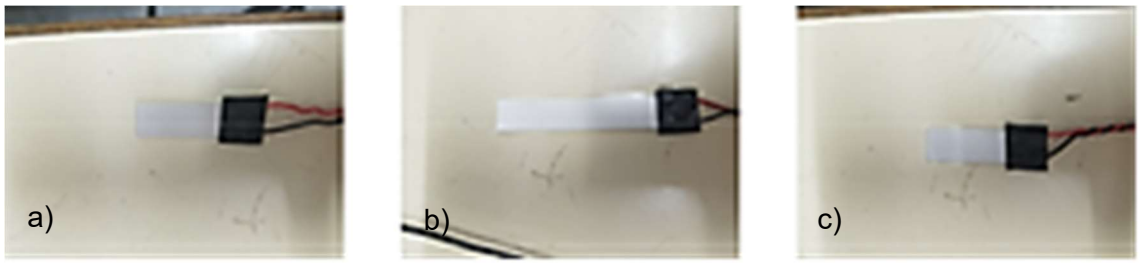

Figure 7 – PVDF piezoelectric devices to be used as fringes: a) device A; b) device B; c) device C.

4.1 Dependency on Wing Reynolds Number and Incidence

Single piezoelectric fringes were attached to the trailing-edge of the wing, as schematically shown in Figure 1a and tested in the wind tunnel, as illustrated in Figure 8. Various nondimensional spanwise locations z/c on the wing (where c is the chord) were analyzed, as significant spatial variability is expected due to the presence of leading-edge tubercles in the finite wing. For a wing aspect ratio of 1.5, the mid-span location corresponds to $z/c = 3/4$.

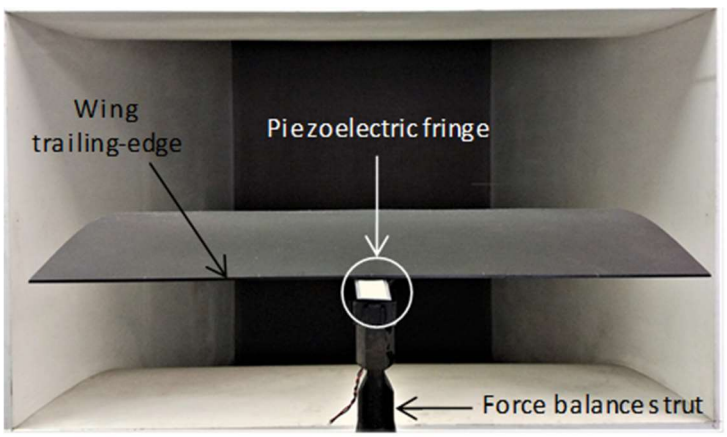

Figure 8 – Wind tunnel setup showing a piezoelectric fringe attached to the trailing-edge, at the mid-span section of the wing.

Fair agreement is obtained between the model predictions in Figure 6b and the results of closed-circuit tests presented in Figure 9 for the investigated Reynolds numbers. The higher power outputs occur at high angle of attack α, an effect which was nevertheless not accounted for in the model. It is interesting to note that, for the outer positions $z/c = [1/4;\ 5/4]$, the highest power outputs occur at an incidence $\alpha = 20°$, while for the inner positions these were attained at a lower angle of attack $\alpha = 15°$. Additionally, it is noticeable that, at low incidence, the harvested power at the outer positions is one or two orders of magnitude lower than at the inner positions. This was visually observed, while running the test, in the way the device oscillated at each angle of attack. At low incidence, almost no oscillations were perceptible, while at high incidence the fringes oscillated strongly. This trend makes a device placed at the outer positions potentially useful for another type of application, namely wake sensing. A device that does not show significant power outputs at low incidence, exhibiting a major increase at high incidence, may be utilized as a sensor to inform the on-board computer that the wing is approaching stall conditions.

Figure 10a demonstrates that device B has a higher energy output at high angle of attack when compared to device A, despite the fact of the open-circuit voltage being lower than for device A. When comparing the values of both devices at low incidence, device A generally generates higher power outputs at the inner positions, while showing a lower output in the outer spanwise positions. The power trends remain largely similar with almost steady values from $\alpha = 0°$ to $\alpha = 10°$, attaining their maxima at $\alpha = 15°$ or $\alpha = 20°$ for the inner positions, staying one order of magnitude lower at low incidence, and then increasing rapidly at high incidence for the outer spanwise positions.

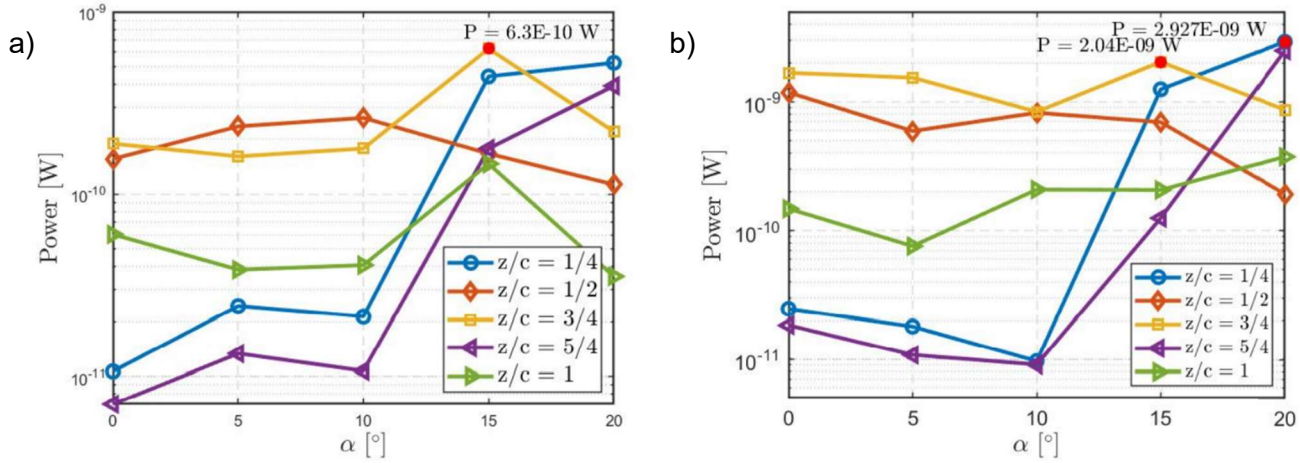

Figure 9 – Power output versus wing incidence in closed-circuit for device A: a) $Re = 70000$; b) $Re = 140000$.

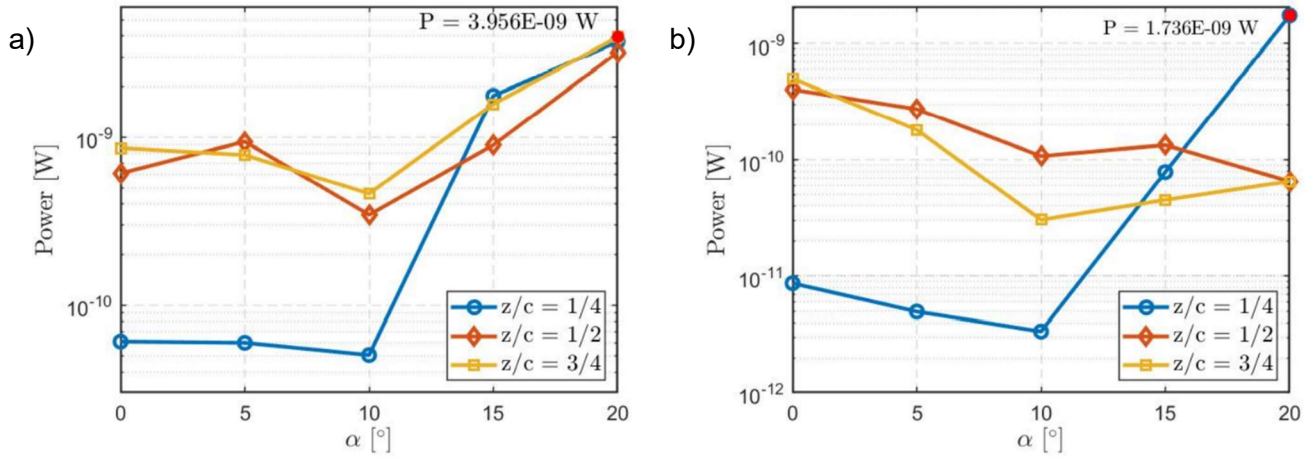

Figure 10 – Power output versus wing incidence at $Re = 140000$ for other devices: a) device B; b) device C.

Device C, characterized by a lower thickness than devices A and B, portrays a few fundamental differences in behavior, as shown in Figure 10b. One can deduce that, unlike the previous devices, device C is more susceptible to undergo larger amplitude oscillations, thus generating more energy at low wing incidence, with the maximum open-circuit voltage measured at $\alpha = 0°$ and $z/c = 3/4$. Additionally, Figure 10b indicates mostly higher power values at $z/c = 1/2$ than at $z/c = 3/4$, which was not the case for the remaining piezoelectric devices. Again, this device seems to perform better at this spanwise position because of its lower thickness. Interestingly, device C provides a maximum power output at $\alpha = 20°$ and $z/c = 1/4$.

4.2 Effect on the Aerodynamic Efficiency of the Wing

Analyzing the effects of the fringes on the overall lift and drag generated by the tubercled wing is relevant because, as stated before, other configurations might be more advantageous in terms of power output at the cost of penalizing the overall aerodynamic efficiency mainly due to a higher resulting drag. The lift and drag forces on the wing were measured with and without the piezoelectric device A (placed at mid-span) for the previous range of angle of attack at $Re = 140000$. The lift-to-drag ratio results are shown in Figure 11. The comparison at $\alpha = 0°$ is surprising, but it is not likely to be accurate, given the large relative uncertainty associated with the (smaller) forces measured with the aerodynamic balance at very low incidence. By ignoring this case in the analysis, a penalty generally results at moderate wing incidence as expected, but a consistent improvement seems to be obtained at high angles of attack, which coincide with near- or post-stall operating conditions [18].

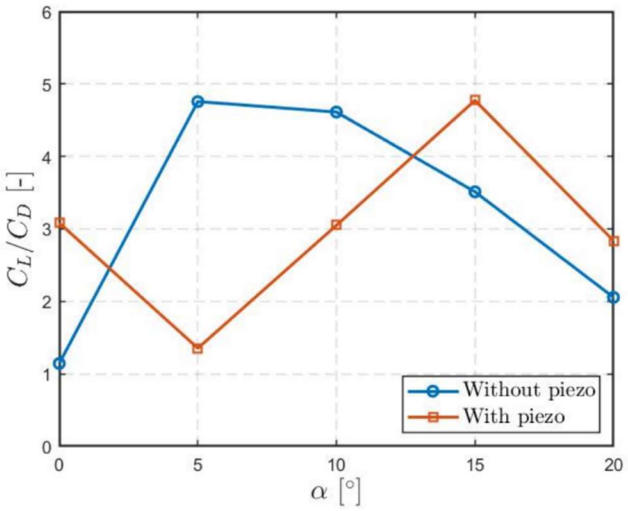

Figure 11 – Aerodynamic efficiency of the tubercled wing with and without the piezoelectric fringe at $Re = 140000$.

4.3 Power Density Ratio

The results obtained across all tests do not boast significantly high power outputs when considering the raw data presented earlier. However, in comparison with other solutions reported in recent studies, these piezoelectric devices are significantly lighter than those. Lighter solutions are favored because these do not carry large weight penalties as a consequence of their added mass. Thus, an analysis on the harvested power per device mass is crucial to draw useful conclusions about the effective performance of the present configuration in a more general context of energy harvesting solutions. Knowing the component characteristics for each device studied here, previous data are now shown in Figures 12 and 13 is terms of power density ratios.

Based on the normalized data, one can conclude that when the fringe mass is taken into account in the analysis, and since all the investigated piezoelectric devices are considerably light, the resulting values for the power density ratio are in the order of 10^{-5} W/kg. Despite generating the highest raw power value, device B exhibits the lowest value of power density ratio in the studied set because it is considerably heavier than devices A and C. Devices A and C show relatively similar results in this analysis because both are characterized by a mass of the same order of magnitude. As a summary, device A has produced the best power density ratio.

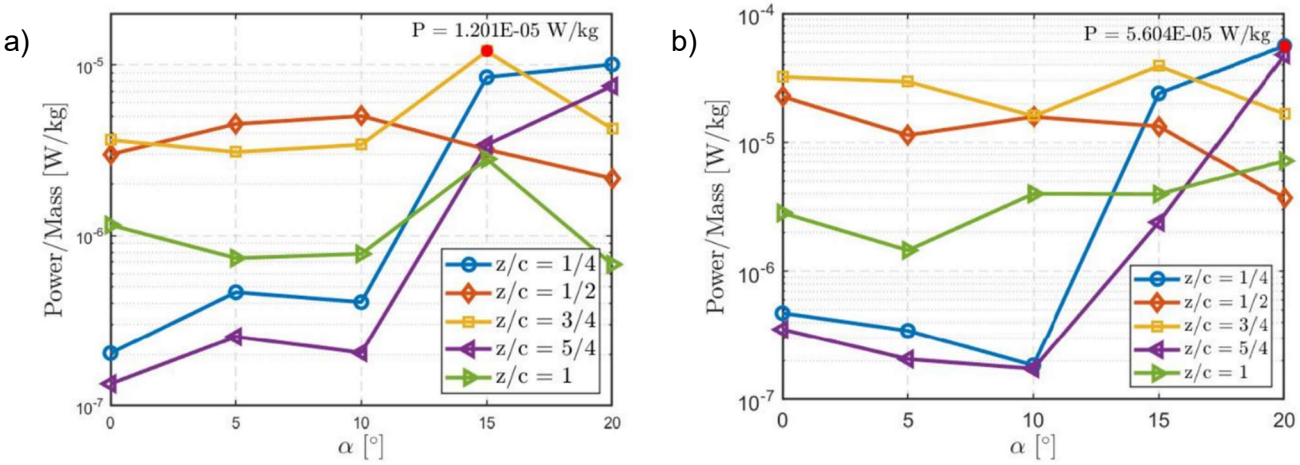

Figure 12 – Power density ratio versus wing incidence for device A: a) $Re = 70000$; b) $Re = 140000$.

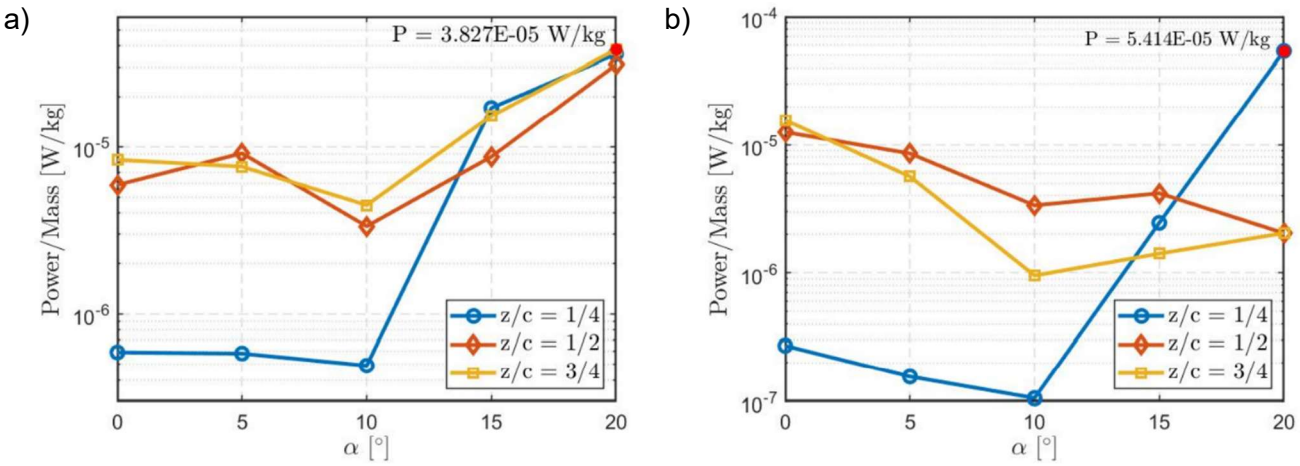

Figure 13 – Power density ratio versus wing incidence at $Re = 140000$ for other devices: a) device B; b) device C.

5. Conclusions

In this work, the energy harvested by a PVDF piezoelectric fringe installed at the trailing-edge of a tubercled wing was quantified. An aero-electro-mechanical model enabled to predict how the device operates at a given Reynolds number. Despite that simplifications were considered in the modeling procedure, fair agreement was found between the model and the experimental results subsequently obtained via wind tunnel testing.

Three different commercially available piezoelectric fringes were experimentally investigated. When comparing the various devices used, a general advantage was found in using the smaller devices A and C, in detriment of the longer device B. Despite showing a higher maximum power output, device B also weighs more than devices A and C, thus resulting in a lower power density ratio. Between devices A and C, the latter characterized by a smaller thickness, device A appears to be a better option for energy harvesting due to its higher power outputs. Nevertheless, taking into consideration the relatively low amounts of power harvested by the piezoelectric fringes, and if not used for energy harvesting purposes, these devices also proved to be useful for the identification of approaching stall conditions, when placed at the outer spanwise locations of the finite wing.

6. Acknowledgements

This work has been supported by Fundação para a Ciência e a Tecnologia (FCT), through IDMEC, under LAETA, project UID/EMS/50022/2019.

7. Copyright Statement

References

[1] Zhao W, Païdoussis MP, Tang L, Liu M and Jiang J. Theoretical and experimental investigations of the dynamics of cantilevered flexible plates subjected to axial flow. *Journal of Sound and Vibration*, Vol. 331, No. 3, pp 575-587, 2012.

[2] Gibbs SC, Wang I and Dowell E. Theory and experiment for flutter of a rectangular plate with a fixed leading edge in three-dimensional axial flow. *Journal of Fluids and Structures*, Vol. 34, pp 68-83, 2012.

[3] Tang L and Païdoussis. On the instability and the post-critical behavior of two-dimensional cantilevered flexible plates in axial flow. *Journal of Sound and Vibration*, Vol. 305, No. 1-2, pp 97-115, 2007.

[4] De Marqui C, Vieira WGR, Erturk A and Inman DJ. Modeling and analysis of piezoelectric energy harvesting from aeroelastic vibrations using the doublet-lattice method. *Journal of Vibration and Acoustics*, Vol. 133, No. 1, pp 011003 (9 pages), 2011.

[5] Abdelke A and Ghommem M. Piezoelectric energy harvesting from morphing wing motions for micro air vehicles. *Theoretical and Applied Mechanics Letters*, Vol. 3, No. 5, pp 052004 (4 pages), 2013.

[6] Bilgen O, Fontenille M and Inman D. Piezoelectric energy harvesting from macro-fiber composites with an application to morphing-wing aircrafts. *19th International Conference on Adaptive Structures and Technologies*, Ascona, Switzerland, pp 339-359, 2008.

[7] Esmaeili A. Experimental and computational investigation of hybrid passive-active stall control for micro aerial vehicles. PhD Thesis, Instituto Superior Técnico, Lisboa, Portugal, 2018.

[8] Song J, Zhao G, Li B and Wang J. Design optimization of PVDF-based piezoelectric energy harvesters. *Heliyon*, Vol. 3, No. 9, pp e00377 (18 pages), 2017.

[9] Rahman M, Lee B-C, Phan D-T and Chung G-S. Fabrication and characterization of highly efficient flexible energy harvesters using PVDF-graphene nanocomposites. *Smart Materials and Structures*, Vol. 22, No. 8, pp 025017, 2013.

[10] Gunasekaran S and Ross G. Effect of piezo-embedded inverted flag in free shear layer wake. *Aerospace*, Vol. 6, No. 3, p 33, 2019.

[11] Boisseau S, Despesse G and Ahmed B. Electrostatic conversion for vibration energy harvesting. *Small Scale Energy Harvesting*. IntechOpen, 2012.

[12] *IEEE Standard on Piezoelectricity*. ANSI/IEEE Std 176-1987, 1988.

[13] Esmaeili A and Sousa JMM. Power density ratio optimization of bimorph piezocomposite energy harvesters using a Multidisciplinary Design Feasible method. *Composite Structures*, Vol. 165, pp 171-179, 2017.

[14] Esmaeili A, Delgado HEC and Sousa JMM. Numerical simulations of low-Reynolds-number flow past finite wings with leading-edge protuberances. *Journal of Aircraft*, Vol. 55, No. 1, pp 226-238, 2018.

[15] Esmaeili A and Sousa JMM. Flow-driven piezoelectric energy harvester on a full-span wing for micro-aerial-vehicle (MAV) application. *Arabian Journal for Science and Engineering*, Vol. 45, pp 5713-5728, 2020.

[16] Kim D, Cosse J, Cerdeira CH and Gharib M. Flapping dynamics of an inverted flag. *Journal of Fluid Mechanics*, Vol. 736, R1, 2013.

[17] Xia Y. Energy harvesting by piezoelectric flags. PhD Thesis, Ecole Polytechnique X, Paris, France, 2015.

[18] Guerreiro JLE and Sousa JMM. Low-Reynolds-number effects in passive stall control using sinusoidal leading edges. *AIAA Journal*, Vol. 50, No. 2, pp 461-469, 2012.